Chem

CellPress

Article

Strain-Induced Corrosion Kinetics at Nanoscale Are Revealed in Liquid: Enabling Control of Corrosion Dynamics of Electrocatalysis

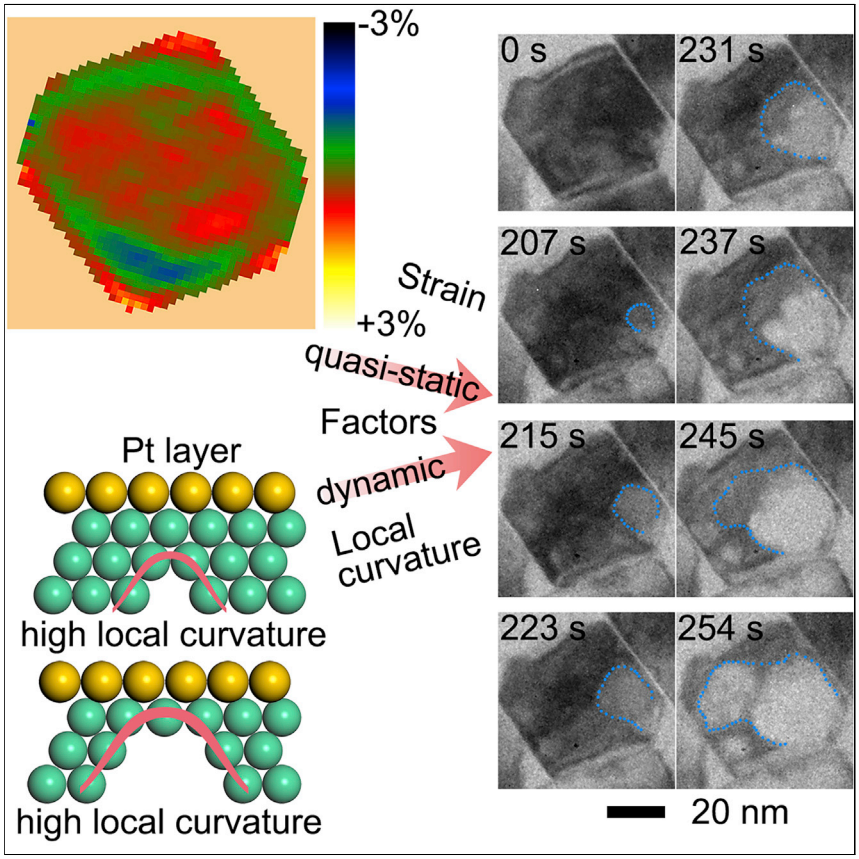

Real-time imaging of the corrosion process of Pd@Pt octahedral electrocatalysts and DFT calculations demonstrate that nanoscale corrosion dynamics are determined both by the quasi-static factor of local strain and by the dynamic factor of local curvature. Strain plays a major role in the early corrosion process, and the local curvature dominates gradually in the later process. This study of corrosion kinetics provides an important design principle for engineering the strains of nanoparticles to achieve corrosion-resistant electrocatalysts.

Fenglei Shi, Wenpei Gao, Hao Shan, ..., Deren Yang, Xiaoqing Pan, Jianbo Wu

msezhanghui@zju.edu.cn (H.Z.)
xiaoqing.pan@uci.edu (X.P.)
jianbowu@sjtu.edu.cn (J.W.)

HIGHLIGHTS

In situ liquid cell TEM is utilized for studying nanoscale corrosion

Both the strain and local curvature control nanoscale corrosion kinetics

Under tensile strain and high local curvature, the etching process is much faster

The newly designed catalyst with smaller strain is corrosion resistant and durable

Shi et al., Chem 6, 2257–2271
September 10, 2020
https://doi.org/10.1016/j.chempr.2020.06.004

Chem

CellPress

Article

Strain-Induced Corrosion Kinetics at Nanoscale Are Revealed in Liquid: Enabling Control of Corrosion Dynamics of Electrocatalysis

Fenglei Shi,[1,8] Wenpei Gao,[2,8] Hao Shan,[1,8] Fan Li,[1] Yalin Xiong,[3] Jiaheng Peng,[1] Qian Xiang,[1] Wenlong Chen,[1] Peng Tao,[1] Chengyi Song,[1] Wen Shang,[1] Tao Deng,[1,4] Hong Zhu,[5,6] Hui Zhang,[3,*] Deren Yang,[3] Xiaoqing Pan,[2,7,*] and Jianbo Wu[1,4,6,9,*]

SUMMARY

Corrosion of nanoparticles during electrocatalysis, such as oxygen reduction reaction (ORR), occurs at the nanoscale and is vital for catalyst stability. Here, using liquid cell (LC) transmission electron microscopy (TEM), we study the corrosion process of palladium@-platinum (Pd@Pt) core-shell octahedra in real time and reveal that both the static local strain and the evolving curvature synergistically control the nanoscale corrosion kinetics. Specifically, in locations with tensile strain and high local curvature, the etching process is much faster. Density functional theory (DFT) calculation suggests that the dissolution potential of the Pd nanocrystal decreases as the strain increases; meanwhile, Pd atoms tend to be corroded more easily on a surface under tensile strain than on one under compressive strain. With these insights on the corrosion mechanism at the nanoscale, we subsequently designed and synthesized nanoparticles with smaller strain, and these showed higher durability in both an *in situ* LC study and an *ex situ* ORR stability test.

INTRODUCTION

Electrocatalysis is the foundation of the modern energy industry. Advanced technologies from energy storage to clean energy conversion involve a wide spectrum of electrochemical processes.[1–7] Examples include the oxygen reduction reaction (ORR)[1,2] and hydrogen oxidation reaction[3] at the cathode and anode in fuel cells, respectively, and the hydrogen evolution reaction[4] and oxygen evolution reaction[5] at the cathode and anode in water splitting, respectively. For these chemical reactions, electrocatalysts are the key to reducing the reaction energy barrier and the electrochemical overpotential, which accelerate the process. However, catalysts degrade under working conditions. During the electrochemical reaction, the electron transfer between chemicals and catalysts causes oxidation or reduction of the surface atoms at the desired potential,[6] which inevitably leads to corrosion. Jeopardizing catalyst stability causes performance degradation. Therefore, developing electrocatalysts with an excellent performance largely depends on the improvement of their stability.

Platinum (Pt)-based nanoparticles, for example, have been widely used as electrocatalysts for various reactions, especially ORR.[7–11] Through facet control,[12] surface composition and strain tuning,[13] frame and cage design,[14] and surface atomic

The Bigger Picture

Corrosion of electrocatalysts during the electrochemical processes is vital for electrocatalysts' stability. Nowadays, nanoparticles are widely used as electrocatalysts for various electrochemical reactions. Hence, it is of great importance to investigate nanoscale corrosion behaviors of nanoparticles. *In situ* liquid cell transmission electron microscopy (LC-TEM) is powerful for studying the dynamics of nanoscale reactions.

This study utilized *in situ* LC-TEM to study the strain-induced nanoscale corrosion and then design and synthesize more stable nanoparticles. The longer-term ambitions of the research are developing promising electrocatalysts with high performance and finally achieving the goal of large-scale commercialization. This study provides insight into electrocatalysts' nanoscale corrosion, which has the potential in the short or long term to make an impact on the design of nanoparticles and further on the energy conversion industry, which is important to society as a whole.

deposition,[15] significant progress has been made on optimizing the initial activity of ORR.[16] Despite this, for most new catalysts, only 10% of the peak performance can be preserved after long-term durability testing on the membrane electrode assembly (MEA) stack.[17] The loss in performance is due to the corrosion of the Pt catalyst at high current density.[17] Understanding how corrosion proceeds in metal nanoparticle catalysts at the atomic scale requires monitoring the entire process with high resolution, which has only recently been possible. *In situ* liquid cell (LC) electron microscopy[18] can capture material evolution,[19–21] including growth,[22–29] phase transition,[30,31] diffusion,[32] and etching,[33–36] in real time.

In our previous work, using *in situ* LC transmission electron microscopy (LC-TEM),[37–40] we studied the corrosion of palladium@platinum (Pd@Pt) cubic core-shell nanoparticles. The process starts with initial etching from exterior defects in corners and terraces.[33] As the corrosion progresses inward, local curvature plays an important role in determining how fast the Pd dissolves inside the nanoparticle. However, in order to improve catalyst stability, controlling local curvature that changes dynamically during corrosion is challenging; it is more feasible to engineer the atomic structure, such as composition and strain. Therefore, to reveal the mechanism of how the atomic structure interplays with local curvature to affect the corrosion dynamics, we performed *in situ* LC-TEM to study the corrosion of Pd@Pt core-shell octahedral nanoparticles, which are among the most active electrocatalysts toward ORR.[13] Combined with theoretical calculation, the results show that the initial progression of corrosion follows the strain landscape and the etching rate is determined by both the strain and the curvature. Furthermore, we designed and synthesized smaller Pd@Pt core-shell octahedral nanoparticles, which had smaller strain and neither dislocations nor defects on the surface layers, as observed in the atomic resolution images. After the *in situ* corrosion experiment and *ex situ* ORR stability test, the new electrocatalysts proved to be more durable.

RESULTS AND DISCUSSION

We prepared Pd@Pt core-shell octahedral nanoparticles by using a liquid phase synthetic approach (see details in the Experimental Procedures).[13] The X-ray diffraction (XRD) of pure Pd, pure Pt, and Pd@Pt core-shell octahedral nanoparticles are shown in Figure S1, which indicates the structure and the purity of the materials. The nanoparticles were pre-loaded into the LC. The LC assembly contained a pair of chips with a gap of 50 nm, allowing the corrosive liquid of 0.1 M NaBr to flow at a rate of 5 μL/min. Figure 1A shows the etching process of a Pd@Pt core-shell octahedron whose side length under projection measures about 37 nm. The sequential *in situ* TEM images show that the visible corrosion started from a terrace site, which is labeled by a red arrow at 240 s. At 274 s, another hole (labeled by an orange arrow) formed and merged with the previous one. As corrosion proceeded, a hole in the upper surface (labeled by a green arrow) also emerged at 282 s. In the next 28 s, the holes merged, and the nanoparticle became a Pt nanocage. In this case, corrosion started from several points during the entire process. The places corresponded to the positions where the defects were. To study how the corrosion proceeded systematically, we focused our analysis on two nanoparticles whose corrosion process started from only one location on the surface (Figures 2 and 3). First, to identify the origin of the corrosion, we characterized the atomic structures of the pristine nanoparticles by high-angle annular dark-field scanning TEM (HAADF-STEM) (Figure 1B). In the Z contrast images, the core-shell nanoparticle had approximately two atomic layers of Pt, enclosing the relatively dimmer Pd atoms in the truncated octahedral core.

[1]State Key Laboratory of Metal Matrix Composites, School of Materials Science and Engineering, Shanghai Jiao Tong University, 800 Dongchuan Road, Shanghai 200240, People's Republic of China

[2]Department of Chemical Engineering and Materials Science, University of California, Irvine, Irvine, CA 92697, USA

[3]State Key Laboratory of Silicon Materials, School of Materials Science & Engineering, Zhejiang University, Hangzhou, Zhejiang 310027, People's Republic of China

[4]Hydrogen Science Research Center, Shanghai Jiao Tong University, Shanghai 200240, People's Republic of China

[5]University of Michigan, Shanghai Jiao Tong University Joint Institute, Shanghai Jiao Tong University, 800 Dongchuan Road, Shanghai 200240, People's Republic of China

[6]Materials Genome Initiative Center, Shanghai Jiao Tong University, Shanghai 200240, People's Republic of China

[7]Department of Physics and Astronomy, University of California, Irvine, Irvine, CA 92697, USA

[8]These authors contributed equally

[9]Lead Contact

*Correspondence: msezhanghui@zju.edu.cn (H.Z.), xiaoqing.pan@uci.edu (X.P.), jianbowu@sjtu.edu.cn (J.W.)

https://doi.org/10.1016/j.chempr.2020.06.004

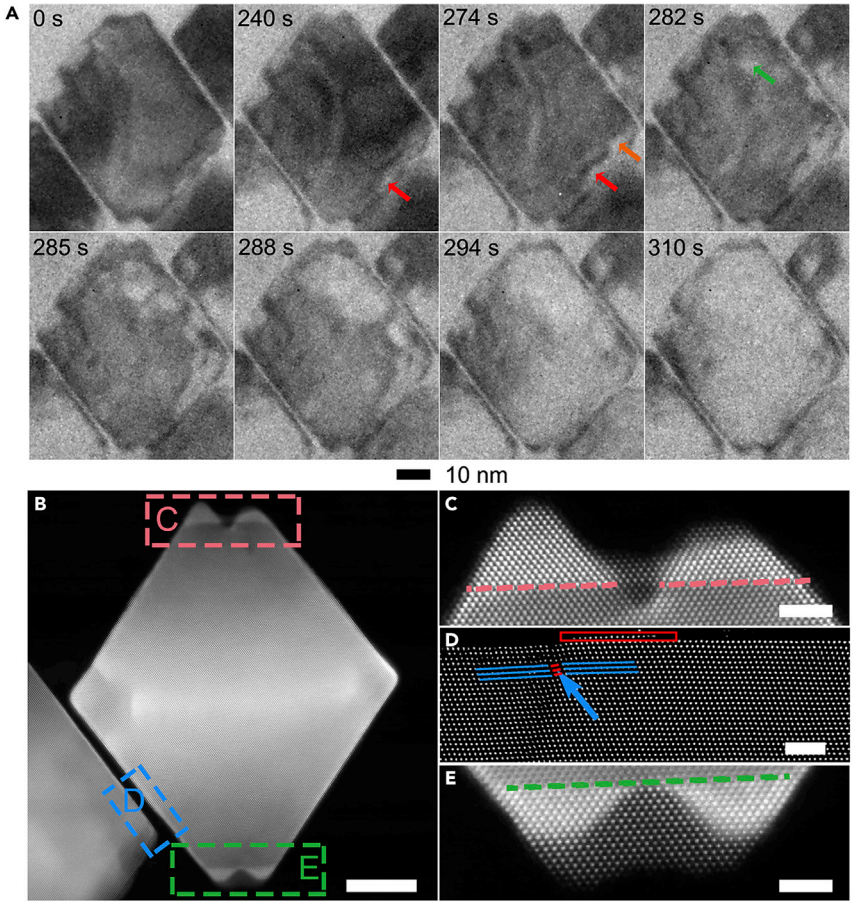

Figure 1. Etching Process and Structure Characterization of a 37 nm Pd@Pt Octahedron

(A) Sequential TEM images showing the etching process of a 37 nm Pd@Pt octahedron.

(B) HAADF-STEM images of a 37 nm Pd@Pt octahedron. The scale bar represents 10 nm.

(C–E) Enlarged views of three regions labeled with dotted boxes in (B). Scale bars represent 2 nm.

There were more Pt layers on the six corners. The Pt surface was under in-plane compression because of the 0.77% lattice mismatch between Pt and Pd, when Pt was epitaxially deposited on Pd.[13] The free energy associated with the strain at the Pd-Pt interface and in the Pt layers increases with larger particle sizes and could create a dislocation on the shell.[41] In our image, the stacking faults form at the {111} terrace to release the strain (Figure 1D). This is consistent with reports that dislocations can exist even inside nanoparticles as small as 10 nm in size.[42] In the red box in Figure 1D, we observe an additional layer of Pt growth starting from the top of the Pd defect, indicating that these defects could further lead to the incomplete coverage of the Pt shell on the surface. Pt atoms also tend to be deposited more on Pd {100}, showing a volcano morphology of Pt layers on the top and bottom corners (Figures 1C and 1E). Missing the protection from Pt layers, these defects on the corners (Figure 1C) and terrace (Figure 1D) are where the corrosion starts.

Meanwhile, because of the different standard reduction potentials of the Pd^{2+}-Pd and Pt^{2+}-Pt pairs,[43] in this Pd@Pt core-shell system, the Pd atoms were etched in the presence of the Br^{-} ions as the anodic reaction (Equation 1). The cathodic reaction proceeded via the reduction of oxidative species generated by the electron

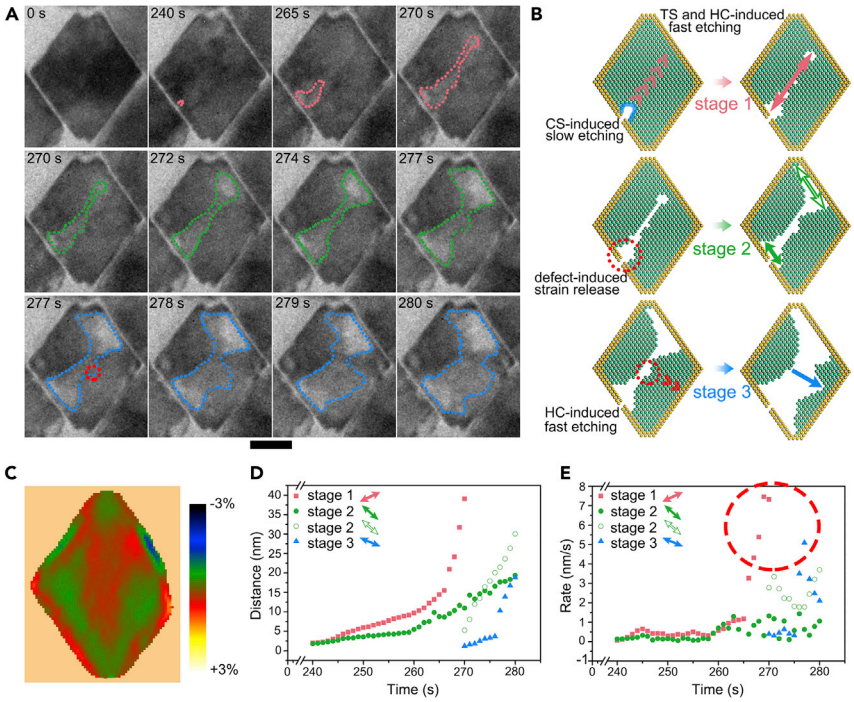

Figure 2. Analysis of a Pd@Pt Octahedron Etching Process Starting from a Terrace Defect

(A) Time-sequential TEM images showing the etching process of a 37 nm Pd@Pt octahedron with a terrace defect. The scale bar represents 20 nm.

(B) Illustration of atomic structures demonstrates the inducements of etching and measured distance at three stages. TS, tensile strain; CS, compressive strain; HC, high curvature.

(C) Strain map of the 37 nm octahedron before corrosion. The color-coded bar represents a range from −3% CS to +3% TS.

(D) Scatter diagrams of measured distance for three stages as a function of time.

(E) The corresponding etching rates of three stages.

beam.[44] The corrosion then proceeded by etching more Pd atoms from the inside. The reaction equation was described as follows:[33]

$$Pd + 4Br^- - 2e^- \rightarrow \left[PdBr_4^{2-}\right] \quad E = 0.49\ V \text{ versus standard hydrogen electrode} \qquad \text{(Equation 1)}$$

In Figure 2A, the corrosion of Pd@Pt octahedra started from the etching of inner Pd atoms at the terrace site as a result of the terrace defects (Figure 1D), where the Br^- ion could access the Pd via the defect. After the pinhole formed near the defect at the interface between Pt and Pd, it then expanded in the Pd part gradually. The entire process proceeded much slower than the corrosion of cubic nanoparticles with terrace defects in our previous report.[33] This difference comes from the closer packing in the Pd (111) planes of octahedra than of Pd (100) in cubes.[45] The corrosion rate during the early stage was determined by how much the corrosive liquid can contact and react with the inner Pd. Before 240 s, the corrosive liquid entered nanoparticles via defects and the area exposed to the corrosive solution was small, resulting in slow corrosion during the early stage. After more volume was etched, the etching accelerated because the larger area was available for reaction. The following visible etching process has three stages (Figure 2A). At the beginning of stage 1, at 240 s, a small pinhole emerged at the site indicated by the red dash line. Then the void could grow along two directions: (1) along the interface between Pd and Pt,

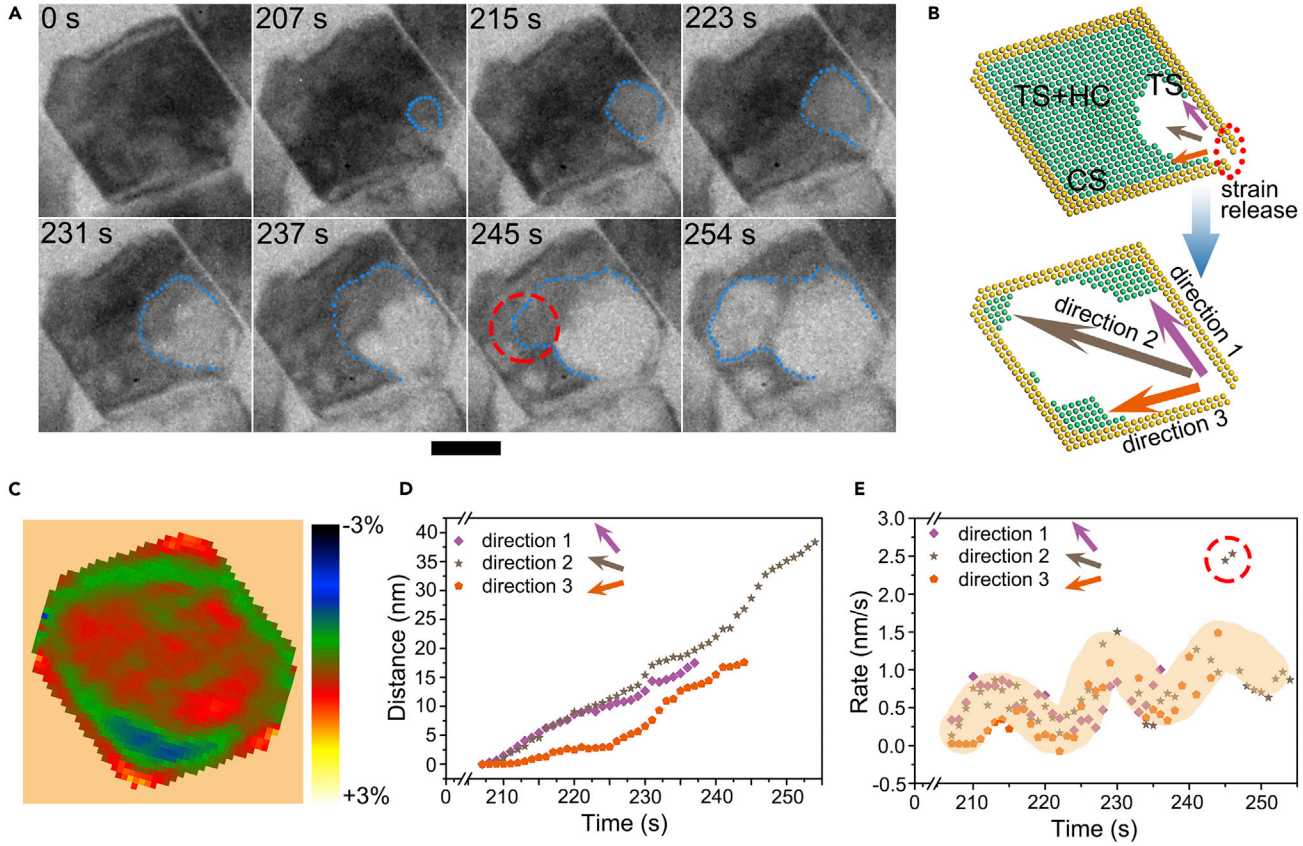

Figure 3. Analysis of a Pd@Pt Octahedron Etching Process Starting from a Corner Defect

(A) Time-sequential TEM images showing the etching process of a 37 nm Pd@Pt octahedron with a corner defect. The scale bar represents 20 nm.

(B) Illustration of atomic structures demonstrates the inducements of etching and measured distance.

(C) Strain map of the 37 nm octahedron before corrosion. The color-coded bar represents a range from −3% CS to +3% TS.

(D) Scatter diagrams of three different directions for measured distance as a function of time.

(E) The corresponding etching rates of three directions.

which was driven by the strain at the interface; and (2) vertically toward the center, determined by both the local curvature[33] and the body strain (Figure 2C). In the *in situ* experiment, we observed that this small cavity expanded to the upper-right (UR) side at 265 s. Subsequently, within 5 s, it expanded significantly at the UR side and formed another pinhole at 270 s. From the strain map of the particle similar in size and shape (Figure 2C), we can interpret that the path of corrosion mostly followed the tensile strain (TS) across the body of the nanoparticle. Stage 1 in Figures 2D and 2E shows that the etching slowly swept from 240 to 265 s with an etching rate of ~0.4 nm/s (see details on the calculation of the etching rate in Figure S2). After 265 s, the etching rate increased to 7.5 nm/s, almost 18 times faster than the initial stage. The fast etching was driven by the synergy of the high curvature (HC) at the tips of the nanochannel and the tensile body strain (Figure 2B, stage 1). Meanwhile, the etching at the lower-left (LL) edge hardly developed at this stage, most likely because of the slightly compressive strain (CS) in that area (Figure 2C).

In stage 2, when the nanochannel reached the UR edge, the large curvature disappeared. Therefore, the interfacial strain became dominant in the corrosion dynamics as these two voids at LL and UR edges grew larger along their interfaces at 272 s, respectively. However, the corrosion at the LL edge was slower than that at the UR

edges (stage 2 in Figures 2D and 2E). It should be noted that the interface strain at these two edges is different. The origin of the interfacial strain between Pt and Pd comes from the lattice mismatch between these metals.[46] Considering that the LL interface contained the terrace defect (Figure 1D), the interface strain at LL site was partially released (Figure 2B, stage 2), which slowed down the strain-driven corrosion at LL site from 240 to 260 s with an etching speed of 0.19 nm/s. On the UR side, the etching rate was higher, from 1.8 to 3.7 nm/s (Figure 2E). The plot of the etching rate followed an "S" shape as a result of the different strains at the UR site. When the etching process came across TS or CS, the etching accelerated; at regions between these two types of strains, the etching slowed down because of the smaller strain. Moreover, the strain in LL and UR sites are CS and TS, respectively, which also resulted in different etching rates in stage 2. From 260 to 280 s, the etching at the LL site also accelerated slightly with a rate of 0.75 nm/s because the CS increased when the etching was far from the terrace defect.

Before and during stage 3, at 274–277 s, the void contour evolved radically with high local curvature (labeled by a red dotted circle at 277 s); the Pd atoms at the lower-right (LR) side were also etched at 280 s. After 277 s, the etching rate quickly ramped from ~0.4 to 5.1 nm/s as a result of the highly curved local contour (the blue arrow). The largest etching rate was almost 12 times faster than the previous stage and then fell down when the etching front approached the Pt shell. From our observation, both the strain and the local curvature can accelerate the corrosion (stage 3 in Figures 2D and 2E), as indicated by the time regions with high etching rates, labeled by a red circle in Figure 2E. The faster etching was due to both HC and strains (TS in stage 1 or CS in stage 3). The synergy of HC and strain accelerated the etching rate; meanwhile, the TS accelerated the corrosion more than CS. Finally, most Pd atoms were etched by 310 s, leaving a Pt octahedral nanocage (Figure S3 and Video S1).

Figure 3A shows the etching of another octahedral Pd@Pt nanoparticle with a corner defect (Figure 1C). At 207 s, a pinhole emerged at the LR corner and expanded until 223 s. The etching propagated to the center of the particle (237 s), and finally, most Pd atoms inside were etched at 254 s. The entire etching process is shown in Figure S4 and Video S2. In this case, the etching directions followed a trident, including one direction along the body diagonal (direction 2) and the other two along the interfaces (directions 1 and 3 in Figure 3B). This corrosion dynamic also highly depended on the strain; there was TS along directions 1 and 2 and CS along direction 3 (Figure 3C). At the earlier stage, the corrosion proceeded isotropically and formed a semispherical corrosion front between the metal and liquid electrolyte. The three corrosion curves almost overlapped during 207–210 s (Figure 3D). After the area with small strain was etched, the corrosion became anisotropic after those three "ridges" of the strain profiles. The etching rates of all the three directions showed fluctuating features (Figure 3E) as a result of the strain distribution inside the nanoparticles. At regions between two different strains, the etching slowed down. Two points at 245 s had a noticeably higher etching rate (labeled by the red circle in Figure 3E) when the newly formed HC accelerated the etching (Figure 3A). The average etching rate along direction 2 was about 0.8 nm/s higher than that of direction 1 (~0.58 nm/s) because the more inert Pt (111) terrace shell could suppress the formation of large concave curvature. The etching rate along direction 3 (0.43 nm/s), however, was lower than that along direction 1 as a result of the different interfacial strains between direction 1 (TS, Figure 3B) and direction 3 (CS, Figure 3B).

According to the cases observed and analyzed above, three factors can influence the corrosion kinetics inside core-shell nanoparticles: (1) interface and defects

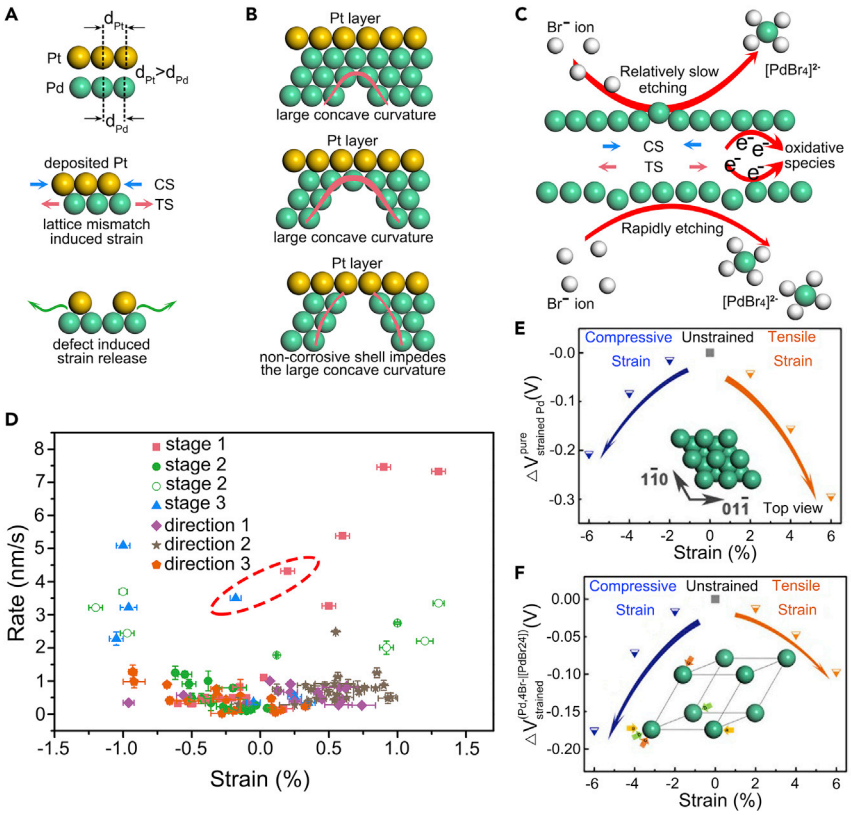

Figure 4. Atomic Illustration of Three Factors that Can Influence the Etching Process and the Calculated Dissolution Electrode Potential Difference

(A) Defect-induced strain release.

(B) Non-corrosive Pt (111) terrace shell impedes the formation of large concave curvature.

(C) Comparison of the etching under CS and TS.

(D) Relationship of etching rate and strain. The positive value means TS.

(E) The calculated dissolution electrode potential difference between Pd (111) slabs and the unstrained Pd (111) slab.

(F) The calculated dissolution electrode potential difference between strained Pd primitive cells and the unstrained Pd primitive cell.

The blue and orange arrows in (E) and (F) guide the eye toward a clear trend.

(Figure 4A), (2) curvature (Figure 4B), and (3) strain (Figure 4C). Some phenomena of the local-curvature-derived etching were partially reported in our previous work.[33] The wide view of nanoparticles during the etching process in LC is shown in Figure S5. The relationship between the etching rate and strain is shown in Figure 4D, which indicates that small strain always has a lower etching rate, whereas large strain (TS or CS) will lead to faster corrosion. Furthermore, TS-induced etching is faster than CS-induced etching. In addition, there are some abnormal points labeled by a red circle in Figure 4D. These points have lower strain but higher etching rates, which is mainly due to the effect of HC. This interesting discovery also proves that the corrosion dynamic is determined by the synergy of strain and local curvature. The highest etching rate (7.5 nm/s) is induced by both HC and TS, which is two orders (375 times) of magnitude higher than the lowest etching rate (0.02 nm/s).

To explain how the etching rate is affected by strain, we used density functional theory (DFT) calculation to compare the dissolution potential of Pd atoms on (111) planes (Figure 4E) and in bulk (Figure 4F). We calculated the dissolution potential

under gradually changing CS and TS by using two strained models for two kinds of Pd atoms in Figure S6A. Figures 4E and 4F indicate that both CS and TS cause a lower dissolution potential for Pd atoms to accelerate the corrosion. It is consistent with the study of the relationship between strain and corrosion of bulk metal (see details in the Supplemental Information section including a brief description of the relationship between strain and corrosion in bulk metal).[47] Nevertheless, the calculated dissolution potential of surface Pd atoms on (111) planes were more related to the real etching surface during the corrosion process (Figure 4E), which showed a faster descent under TS, indicating easier etching under TS than under CS. Generally, both TS and CS promote the etching process. The etching rate is related to the bonding environment of surface atoms. Under in-plane CS, the bond length among the surface atoms is shorter. However, the bond length with the atoms in layers underneath is larger, making the interlayer interaction weaker. With TS, the stretching of the atomic bond among the atoms in the same plane makes it easier to react with the etching species. Thus, which strain will facilitate etching more depends on whether the in-plane bonding or the out-of-plane bonding plays the more important role. For Pd atoms on the (111) surface, the coordination number is 9, including the six nearest atoms in plane and three atoms out of plane. Under TS, the stretched bonds among the six atoms leave the surface atoms easier to etch than those under the compressive in-plane strain.

Thus, the nanoscale kinetics of Pd@Pt octahedra corrosion have been analyzed. The etching started from the defects on the corners and terrace, which was attributed to the incomplete diffusion and accumulated strain of the Pd and Pt lattice mismatch. After that, the etching liquid entered into the interior of the octahedron and the corrosion was guided by the strain. The lattice-mismatch-induced strain accelerated the corrosion rate during the etching process because the strain led to a decrease in the metal equilibrium potential and sequentially made the metal be more easily etched. In areas with defects, the adjacent interface strain released and led different etching kinetics. Finally, our quantitative study showed that TS promoted the corrosion more violently than CS at the nanoscale, which has not been observed before.[48] In analyzing how the corrosion process is influenced by the strain distribution at the early stage, we considered only the body strain (internal strain) before the etching. As the etching front interacts with the exposed surface during corrosion, the major part of the particle body remains the same structure, so the strain will not change significantly. Later in the process, when the majority of the particle is etched, the change of strain will be larger, and meanwhile, the local curvature will dominate the dynamics because the body strain will not remain.

Therefore, the local curvature evolution can also influence the corrosion behavior dynamically. At the atomic scale, the local curvature is correlated with the index of the crystal plane. High local curvature is related to high-index surface planes, which consist of atoms with a low coordination number. The bondings of these atoms with the others are relatively weak, so they are etched more easily and more rapidly.[33] The local curvature can also be influenced when meeting the Pt shell; the inert Pt (111) layer will flatten the local curvature and reduce the corrosion rate.

According to the nanoscale corrosion mechanism discussed above, we designed and synthesized a more stable Pd@Pt core-shell octahedral nanoparticle with strain control. By adjusting the size of the Pd octahedral core and the amount of Pt precursor, we prepared a smaller Pd@Pt octahedron with an edge length of 8 nm. Figure 5A shows the HAADF-STEM image of an 8 nm Pd@Pt core-shell octahedron. Noticeably, the strain mapping (Figure 5B) indicates that our strain-designed nanoparticles

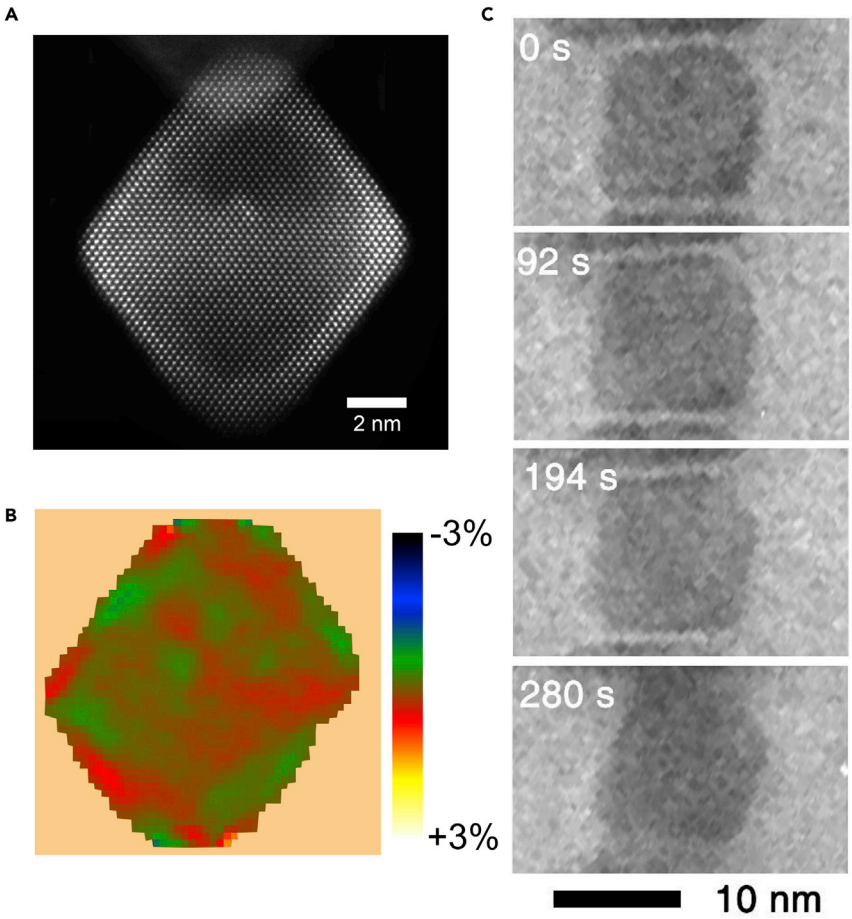

Figure 5. Structure Characterization, Corresponding Strain Mapping, and Etching Process of an 8 nm Pd@Pt Octahedron

(A) HAADF-STEM images of an 8 nm Pd@Pt octahedron.

(B) Strain map of the 8 nm octahedron before corrosion. The color-coded bar represents a range from −3% CS to +3% TS.

(C) Sequential TEM images showing an unetched 8 nm Pd@Pt octahedron in corrosive liquid.

had much smaller intrinsic strain than the larger ones. To confirm the uniformity of the small nanoparticles, both low-magnification STEM images and atomic-resolution images of the small nanoparticles are shown in Figures S7A–S7E. These small nanoparticles have complete Pt layers, and there are no dislocations or defects on the surface layers. In addition, the average value of the strain in nanoparticles with different sizes is also shown in Figure S7F, indicating that small nanoparticles have lower strain. Figure S7 shows the uniformity of the small nanoparticles. Figure 5C shows the sequential *in situ* TEM images of one nanoparticle captured in the corrosive liquid (Video S3). It was stable given that no obvious corrosion occurred.

To further confirm the stability of the 8 nm Pd@Pt octahedron in a real electrochemical test, we carried out accelerated durability testing (ADT) for 20,000 cycles in 0.1 M $HClO_4$ solution. Figures 6A and 6B show the ORR polarization curves of 8 and 37 nm octahedral nanoparticles before and after ADT, respectively. The 8 nm nanoparticle has a much smaller loss in half-wave potential (HP) (0.06 $\pm$ 0.01 mV) than the 37 nm nanoparticles (32.37 $\pm$ 0.08 mV), indicating a more durable ORR performance (Figure 6E). Furthermore, the loss of kinetic current density (j_K, measured at 0.9 V versus

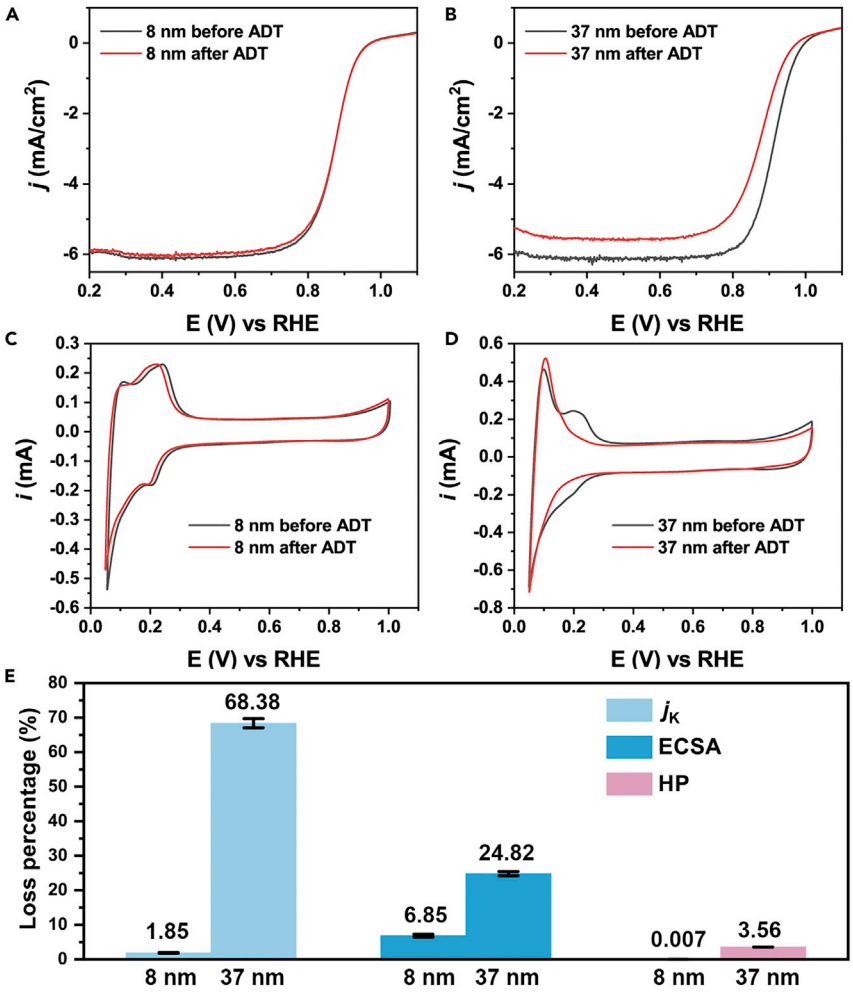

Figure 6. *Ex Situ* Electrochemical Durability Testing and Activity Loss

(A and B) ORR polarization curves of 8 nm (A) and 37 nm (B) Pd@Pt octahedra before and after 20,000 cycles of ADT.

(C and D) CV curves of 8 nm (C) and 37 nm (D) Pd@Pt octahedra before and after 20,000 cycles of ADT.

(E) Loss percentage of kinetic current density (j_K), electrochemical active surface area (ECSA), and half-wave potential (HP).

reversible hydrogen electrode) of the 8 and 37 nm catalysts was 1.85% ± 0.1% and 68.38% ± 1.3%, respectively, indicating a better durability performance of the 8 nm Pd@Pt octahedron (Figure 6E). Figures 6C and 6D show the cyclic voltammetry (CV) curves of the 8 and 37 nm Pd@Pt octahedra before and after 20,000 cycles of ADT. The corresponding electrochemical active surface area (ECSA) of the 8 nm Pd@Pt octahedron had a loss of 2.58 ± 0.18 m^2/g_{Pt} (6.85% ± 0.4% loss; Figure 6E) after ADT, whereas 37 nm Pd@Pt octahedron had a loss of 10.42 ± 0.37 m^2/g_{Pt} (24.82% ± 0.6% loss; Figure 6E). All of the mean specific values of the activities are also shown in Table S3. The *ex situ* ORR stability testing finally confirmed that our strain-designed catalysts were more durable not only in the *in situ* corrosion experiment but also in the real electrochemical test. It is worth mentioning that there is an unavoidable gap between the *in situ* TEM observation on a limited number of nanoparticles and *ex situ* electrochemical measurements of an ensemble of nanoparticles. The gap is from the difference in environments, reactor spaces, catalyst support,

and beam effect. Here, we confirmed the uniformity of the materials by using larger sampling and extracted general behaviors of corrosion at the nanoscale by repeating the *in situ* experiments.

Conclusion

In summary, we imaged the real-time corrosion process of Pd@Pt octahedra and the formation of the Pt nanocages by using LC-TEM. The corrosion dynamics are determined by both the local strain and the evolving curvature. Strain plays a major role in the early corrosion process, and the local curvature dominates gradually in the later process. With TS and high local curvature, the corrosion of Pd is accelerated. The highest etching rate can reach 7.5 nm/s under the synergy of both TS and high local curvature; with only one of these two factors, the etching rates are about 2.5 nm/s, indicating that the extent of how each factor changes the kinetics can be similar. On the basis of the understanding of these mechanistic insights, strain-designed nanoparticles exhibited higher durability in performance for both the *in situ* corrosion experiment and the *ex situ* ORR stability test. Therefore, the study of corrosion kinetics provides an important design principle for engineering the strains of the nanoparticles to achieve corrosion-resistant electrocatalysts.

EXPERIMENTAL PROCEDURES

Resource Availability

Lead Contact

Further information and requests for resources should be directed to and will be fulfilled by the Lead Contact, Jianbo Wu (jianbowu@sjtu.edu.cn).

Materials Availability

This study did not generate new unique materials.

Data and Code Availability

This study did not generate or analyze datasets or code.

Chemicals and Materials

Poly(vinylpyrrolidone) (PVP, Mw ≈ 55,000), sodium tetrachloropalladate (Na_2PdCl_4, 99.9%), chloroplatinic acid (H_2PtCl_6, 99.9%), potassium bromide (KBr), ascorbic acid (AA), potassium chloride (KCl), sodium bromide (NaBr), and butylamine (98%) were ordered from Sigma Aldrich company. Dodecylamine (98%) and oleylamine (OAm, 80%–90%) were ordered from Aladdin company. Toluene, formaldehyde (HCHO, 37%–40%), ethanol, methanol, n-butylamine, isopropanol, acetone, and cyclohexane were ordered from Sinopharm Chemical Reagent company. Deionized water (18.2 MΩ·cm).

Synthesis of Pd Nanocubes

The Pd nanocubes were generated according to the reported work.[13] In a typical synthesis, 105 mg PVP, 400 mg KBr, 60 mg AA, and 8.0 mL deionized (DI) water were added in a 20 mL glass vial and mixed. Then, the mixed solution was heated to 80°C under magnetic stirring for 5–10 min. Then, 3 mL DI water containing 57 mg Na_2PdCl_4 was quickly added into the mixed solution by a pipette. The reaction was kept at 80°C for 3 h. After the solution cooled to room temperature, the sample was washed with ethanol and acetone three times by a centrifuge. Finally, the samples were re-dispersed in ethanol solution for further use.

Synthesis of Pd Octahedra

The Pd octahedral seeds were synthesized according to the previous work.[13] In a typical synthesis, 100 μL HCHO, 105 mg PVP, and 0.2 mL DI water containing cubic

Pd seeds were dispersed into 8 mL DI water and then heated to 60°C for 5 min. Then, 3 mL DI water containing 20 mg Na_2PdCl_4 was quickly added into the mixed solution and kept at 60°C for 3 h. After the mixed solution cooled to room temperature, the sample was washed with ethanol and acetone three times by a centrifuge. Finally, the samples were re-dispersed in ethanol solution for further use.

Phase Transfer of Pd Octahedra

In a typical process, 8 mL ethanol containing Pd octahedral nanoparticles was mixed with 3 mL toluene and 5 mL OAm in a 20 mL glass vial. The phase transfer was proceeded by magnetic stirring of the mixed solution at 80°C for 10 h. The samples were washed with ethanol by a centrifuge and then re-dispersed in OAm, which served as the octahedral seeds for the growth of Pt layers.

Epitaxial Growth of Pt Layers

In a typical synthesis, 4 mL OAm containing octahedral Pd seeds was injected into a 25 mL single-necked flask and heated to 180°C by oil bath for 10 min. Then, 2 mL OAm containing a certain amount of H_2PtCl_6 was injected into the flask. The reaction was kept at 180°C for 3 h. The final product was obtained by being washed with ethanol and cyclohexane several times by a centrifuge.

Morphological, Structural, Compositional, and Strain Characterizations

HAADF-STEM was taken on a JEOL ARM300CF aberration-corrected scanning transmission electron microscope at 300 kV. The model of the aberration corrector was CEOS GmbH. The size of the octahedra was defined by the edge length of the nanoparticles in TEM images. The strain-mapping analysis was carried out with Digital Micrograph software. XRD patterns were taken on a Rigaku Smart Lab X-Ray Diffractometer.

In Situ TEM Characterization

This work used a LC-TEM holder called Poseidon 500 (Protochips, USA). Generally, a pair of E-chips were utilized for preparing the cell. The LC had a 50 nm space and allowed the corrosive liquid to flow at a rate of 300 μL/h via a syringe pump (Harvard Apparatus, Pump 11 Elite). Before loading, the photoresist on each E-chip needed to be removed by acetone and methanol. Afterward, we dried the E-chips with compressed air and then cleaned them with oxygen plasma (Gatan, Model 950) for 3 min to remove the contamination and make the surfaces hydrophilic. We added the gasket into its pocket and then placed the small E-chip on the tip of the holder and added 1–2 μL of the sample solution with a pipette. Finally, the large E-chip was put onto the small E-chip with its membrane side down, and then the screws were tightened. Leak check was then performed by a vacuum pump. After the leak check was passed, the holder was inserted into the transmission electron microscope. The *in situ* TEM imaging was obtained by a JEOL JEM2100 (JEOL, Tokyo, Japan) at a voltage of 200 kV. Videos were recorded by a Cantega G2 camera (Olympus, Japan). All images analysis was conducted on the original images extracted from the recorded videos. Figure S5 and Video S4 show corrosion in a wide view. Particles a and b had corner and terrace defects, respectively. We used ImageJ software to measure the etching distance.

Strain Mapping

Atomic-resolution HAADF-STEM images of Pd@Pt nanoparticles were taken on JEOL ARM300CF aberration-corrected scanning transmission electron microscope at 300 kV. The position of each atomic column in the STEM images was based on a template

matching method (TeMA):[49] the image of a single atomic column was first selected as a template, which was then fitted with every sub-area in a consistent manner for the entire image via cross-correlation. The peak positions in the cross-correlation map indicated the atom locations. By minimizing the deviation of the measured atomic position from the reference lattice and recording the atom displacement from this reference, we could map local strain (ϵ) at atomic resolution.

DFT Calculation

The detailed DFT method is described in the Supplemental Information.

Ex Situ Electrochemical Testing

The detailed carbon-supported electrocatalyst preparation and electrochemical measurement are described in the Supplemental Information.

SUPPLEMENTAL INFORMATION

Supplemental Information can be found online at https://doi.org/10.1016/j.chempr.2020.06.004.

ACKNOWLEDGMENTS

This work was sponsored by the National Key R&D Program of China (2017YFB0406000), the National Science Foundation of China (21875137, 51521004, 51522103, 51871200, 61721005, and 51420105009), the Innovation Program of Shanghai Municipal Education Commission (project 2019-01-07-00-02-E00069), the 111 Project (project B16032), and the Center of Hydrogen Science and Joint Research Center for Clean Energy Materials at Shanghai Jiao Tong University. H.Z. acknowledges financial support from Shanghai Automotive Industry Corporation (1714) and the use computing resources from the Shanghai Jiao Tong University Supercomputer Center. H.Z. thanks the National Program for Support of Top-notch Young Professionals at Zhejiang University. X.P. acknowledges sponsors from National Science Foundation grants (CBET-1159240 and DMR-1506535). *In situ* TEM was operated at the facilities in the MSE at Shanghai Jiao Tong University, and STEM work was conducted at the facilities of the Irvine Materials Research Insititute at the University of California, Irvine. The authors also thank Peter Tieu, Mingjie Xu, and Tom Lee for their help with material characterizations and manuscript writing.

AUTHOR CONTRIBUTIONS

Conceptualization, F.S. and J.W.; Methodology, F.S., H.S., W.G., F.L., and H.Z.; Resources, F.S. and Y.X.; Formal Analysis, W.G., Q.X., J.P., and W.C.; Writing – Original Draft, F.S., W.G., and H.S.; Writing – Review & Editing, W.S., P.T., C.S., T.D., and J.W.; Supervision, D.Y., H.Z., X.P., and J.W.; Funding Acquisition, H.Z., T.D., X.P., and J.W.

DECLARATION OF INTERESTS

The authors declare no competing interests.

Received: November 30, 2019
Revised: January 30, 2020
Accepted: June 2, 2020
Published: June 26, 2020

REFERENCES

1. Wu, J., and Yang, H. (2013). Platinum-based oxygen reduction electrocatalysts. Acc. Chem. Res. *46*, 1848–1857.
2. Nørskov, J.K., Rossmeisl, J., Logadottir, A., Lindqvist, L., Kitchin, J.R., Bligaard, T., and Jónsson, H. (2004). Origin of the overpotential for oxygen reduction at a fuel-cell cathode. J. Phys. Chem. B *108*, 17886–17892.
3. Jiao, Y., Zheng, Y., Jaroniec, M., and Qiao, S.Z. (2015). Design of electrocatalysts for oxygen- and hydrogen-involving energy conversion reactions. Chem. Soc. Rev. *44*, 2060–2086.
4. Hinnemann, B., Moses, P.G., Bonde, J., Jørgensen, K.P., Nielsen, J.H., Horch, S., Chorkendorff, I., and Nørskov, J.K. (2005). Biomimetic hydrogen evolution: MoS2 nanoparticles as catalyst for hydrogen evolution. J. Am. Chem. Soc. *127*, 5308–5309.
5. Mccrory, C.C.L., Jung, S., Peters, J.C., and Jaramillo, T.F. (2013). Benchmarking heterogeneous electrocatalysts for the oxygen evolution reaction. J. Am. Chem. Soc. *135*, 16977–16987.
6. Seh, Z.W., Kibsgaard, J., Dickens, C.F., Chorkendorff, I., Nørskov, J.K., and Jaramillo, T.F. (2017). Combining theory and experiment in electrocatalysis: insights into materials design. Science *355*, eaad4998.
7. Yu, W., Porosoff, M.D., and Chen, J.G. (2012). Review of Pt-based bimetallic catalysis: from model surfaces to supported catalysts. Chem. Rev. *112*, 5780–5817.
8. Gasteiger, H.A., Kocha, S.S., Sompalli, B., and Wagner, F.T. (2005). Activity benchmarks and requirements for Pt, Pt-alloy, and non-Pt oxygen reduction catalysts for PEMFCs. Appl. Catal. B *56*, 9–35.
9. Chen, J., Lim, B., Lee, E.P., and Xia, Y. (2009). Shape-controlled synthesis of platinum nanocrystals for catalytic and electrocatalytic applications. Nano Today *4*, 81–95.
10. Wu, J., Qi, L., You, H., Gross, A., Li, J., and Yang, H. (2012). Icosahedral platinum alloy nanocrystals with enhanced electrocatalytic activities. J. Am. Chem. Soc. *134*, 11880–11883.
11. Wu, J., Li, P., Pan, Y.T., Warren, S., Yin, X., and Yang, H. (2012). Surface lattice-engineered bimetallic nanoparticles and their catalytic properties. Chem. Soc. Rev. *41*, 8066–8074.
12. Wu, J., Gross, A., and Yang, H. (2011). Shape and composition-controlled platinum alloy nanocrystals using carbon monoxide as reducing agent. Nano Lett *11*, 798–802.
13. Xiong, Y., Shan, H., Zhou, Z., Yan, Y., Chen, W., Yang, Y., Liu, Y., Tian, H., Wu, J., Zhang, H., and Yang, D. (2017). Tuning surface structure and strain in Pd–Pt core–shell nanocrystals for enhanced electrocatalytic oxygen reduction. Small *13*, 1603423.
14. Zhang, L., Roling, L.T., Wang, X., Vara, M., Chi, M., Liu, J., Choi, S.I., Park, J., Herron, J.A., Xie, Z., et al. (2015). Nanocatalysts. Platinum-based nanocages with subnanometer-thick walls and well-defined, controllable facets. Science *349*, 412–416.
15. Bian, T., Zhang, H., Jiang, Y., Jin, C., Wu, J., Yang, H., and Yang, D. (2015). Epitaxial growth of twinned Au–Pt core–shell star-shaped decahedra as highly durable electrocatalysts. Nano Lett *15*, 7808–7815.
16. Papageorgopoulos, D. (2010). DOE fuel cell technology program overview and introduction to the 2010 fuel cell pre-solicitation workshop in doe fuel cell pre-solicitation workshop (Office of Energy Efficiency & Renewable Energy).
17. Schmittinger, W., and Vahidi, A. (2008). A review of the main parameters influencing long-term performance and durability of PEM fuel cells. J. Power Sources *180*, 1–14.
18. Shi, F., Li, F., Ma, Y., Zheng, F., Feng, R., Song, C., Tao, P., Shang, W., Deng, T., and Wu, J. (2019). In situ transmission electron microscopy study of nanocrystal formation for electrocatalysis. ChemNanoMat *5*, 1439–1455.
19. Wu, J., Shan, H., Chen, W., Gu, X., Tao, P., Song, C., Shang, W., and Deng, T. (2016). In situ environmental TEM in imaging gas and liquid phase chemical reactions for materials research. Adv. Mater. *28*, 9686–9712.
20. Huang, J.Y., Zhong, L., Wang, C.M., Sullivan, J.P., Xu, W., Zhang, L.Q., Mao, S.X., Hudak, N.S., Liu, X.H., Subramanian, A., et al. (2010). In situ observation of the electrochemical lithiation of a single SnO2 nanowire electrode. Science *330*, 1515–1520.
21. Liu, X.H., Wang, J.W., Huang, S., Fan, F., Huang, X., Liu, Y., Krylyuk, S., Yoo, J., Dayeh, S.A., Davydov, A.V., et al. (2012). In situ atomic-scale imaging of electrochemical lithiation in silicon. Nat. Nanotechnol. *7*, 749–756.
22. Wu, J., Gao, W., Wen, J., Miller, D.J., Lu, P., Zuo, J.M., and Yang, H. (2015). Growth of Au on Pt icosahedral nanoparticles revealed by low-dose in situ TEM. Nano Lett *15*, 2711–2715.
23. Gamalski, A.D., Tersoff, J., and Stach, E.A. (2016). Atomic resolution in situ imaging of a double-bilayer multistep growth mode in gallium nitride nanowires. Nano Lett *16*, 2283–2288.
24. Li, D., Nielsen, M.H., Lee, J.R., Frandsen, C., Banfield, J.F., and De Yoreo, J.J. (2012). Direction-specific interactions control crystal growth by oriented attachment. Science *336*, 1014–1018.
25. Nielsen, M.H., Aloni, S., and De Yoreo, J.J. (2014). In situ TEM imaging of CaCO3 nucleation reveals coexistence of direct and indirect pathways. Science *345*, 1158–1162.
26. Smeets, P.J., Cho, K.R., Kempen, R.G., Sommerdijk, N.A., and De Yoreo, J.J. (2015). Calcium carbonate nucleation driven by ion binding in a biomimetic matrix revealed by in situ electron microscopy. Nat. Mater. *14*, 394–399.
27. Liao, H.G., Cui, L., Whitelam, S., and Zheng, H. (2012). Real-time imaging of Pt3Fe nanorod growth in solution. Science *336*, 1011–1014.
28. Liao, H.G., Zherebetskyy, D., Xin, H., Czarnik, C., Ercius, P., Elmlund, H., Pan, M., Wang, L.W., and Zheng, H. (2014). Nanoparticle growth. Facet development during platinum nanocube growth. Science *345*, 916–919.
29. Ma, Y., Gao, W., Shan, H., Chen, W., Shang, W., Tao, P., Song, C., Addiego, C., Deng, T., Pan, X., and Wu, J. (2017). Platinum-based nanowires as active catalysts toward oxygen reduction reaction: in situ observation of surface-diffusion-assisted, solid-state oriented attachment. Adv. Mater. *29*, 1703460.
30. Chen, L., Liu, J., Jiang, C., Zhao, K., Chen, H., Shi, X., Chen, L., Sun, C., Zhang, S., Wang, Y., and Zhang, Z. (2018). Nanoscale behavior and manipulation of the phase transition in single-crystal Cu2Se. Adv. Mater. *31*, e1804919.
31. Grogan, J.M., Schneider, N.M., Ross, F.M., and Bau, H.H. (2014). Bubble and pattern formation in liquid induced by an electron beam. Nano Lett *14*, 359–364.
32. Zhu, G., Jiang, Y., Lin, F., Zhang, H., Jin, C., Yuan, J., Yang, D., and Zhang, Z. (2014). In situ study of the growth of two-dimensional palladium dendritic nanostructures using liquid-cell electron microscopy. Chem. Commun. *50*, 9447–9450.
33. Shan, H., Gao, W., Xiong, Y., Shi, F., Yan, Y., Ma, Y., Shang, W., Tao, P., Song, C., Deng, T., et al. (2018). Nanoscale kinetics of asymmetrical corrosion in core-shell nanoparticles. Nat. Commun. *9*, 1011.
34. Jiang, Y., Zhu, G., Lin, F., Zhang, H., Jin, C., Yuan, J., Yang, D., and Zhang, Z. (2014). In situ study of oxidative etching of palladium nanocrystals by liquid cell electron microscopy. Nano Lett *14*, 3761–3765.
35. Wu, J., Gao, W., Yang, H., and Zuo, J.M. (2017). Dissolution kinetics of oxidative etching of cubic and icosahedral platinum nanoparticles revealed by in situ liquid transmission electron microscopy. ACS Nano *11*, 1696–1703.
36. Ye, X., Jones, M.R., Frechette, L.B., Chen, Q., Powers, A.S., Ercius, P., Dunn, G., Rotskoff, G.M., Nguyen, S.C., Adiga, V.P., et al. (2016). Single-particle mapping of nonequilibrium nanocrystal transformations. Science *354*, 874–877.
37. Ross, F.M. (2015). Opportunities and challenges in liquid cell electron microscopy. Science *350*, aaa9886.
38. De Jonge, N., and Ross, F.M. (2011). Electron microscopy of specimens in liquid. Nat. Nanotechnol. *6*, 695–704.
39. De Jonge, N., Peckys, D.B., Kremers, G.J., and Piston, D.W. (2009). Electron microscopy of whole cells in liquid with nanometer resolution. Proc. Natl. Acad. Sci. USA *106*, 2159–2164.
40. Park, J., Elmlund, H., Ercius, P., Yuk, J.M., Limmer, D.T., Chen, Q., Kim, K., Han, S.H., Weitz, D.A., Zettl, A., and Alivisatos, A.P. (2015). Nanoparticle imaging. 3D structure of individual nanocrystals in solution by electron microscopy. Science *349*, 290–295.
41. Freund, L.B., and Suresh, S. (2003). Thin Film Materials: Stress, Defect Formation, and

Surface Evolution (Cambridge University Press).

42. Chen, C.C., Zhu, C., White, E.R., Chiu, C.Y., Scott, M.C., Regan, B.C., Marks, L.D., Huang, Y., and Miao, J. (2013). Three-dimensional imaging of dislocations in a nanoparticle at atomic resolution. Nature *496*, 74–77.

43. Haynes, W.M. (2012). CRC Handbook of Chemistry and Physics, 95th Edition (CRC Press).

44. Schneider, N.M., Norton, M.M., Mendel, B.J., Grogan, J.M., Ross, F.M., and Bau, H.H. (2014). Electron–water interactions and implications for liquid cell electron microscopy. J. Phys. Chem. C *118*, 22373–22382.

45. Chung, D.Y., Jun, S.W., Yoon, G., Kwon, S.G., Shin, D.Y., Seo, P., Yoo, J.M., Shin, H., Chung, Y.H., Kim, H., et al. (2015). Highly durable and active PtFe nanocatalyst for electrochemical oxygen reduction reaction. J. Am. Chem. Soc. *137*, 15478–15485.

46. Zhang, H., Jin, M., and Xia, Y. (2012). Enhancing the catalytic and electrocatalytic properties of Pt-based catalysts by forming bimetallic nanocrystals with Pd. Chem. Soc. Rev. *41*, 8035–8049.

47. Zhou, C.H., Ma, H.T., and Wang, L. (2010). Comparative study of oxidation kinetics for pure nickel oxidized under tensile and compressive stress. Corros. Sci. *52*, 210–215.

48. Evans, H.E. (1995). Stress effects in high temperature oxidation of metals. Int. Mater. Rev. *40*, 1–40.

49. Zuo, J.M., Shah, A.B., Kim, H., Meng, Y., Gao, W., and Rouviére, J.L. (2014). Lattice and strain analysis of atomic resolution z-contrast images based on template matching. Ultramicroscopy *136*, 50–60.